Available online at www.sciencedirect.com
SCIENCE DIRECT®
Acta Materialia 53 (2005) 1041–1049
Acta MATERIALIA
www.actamat-journals.com

Quantitative determination of strain fields around Ni_4Ti_3 precipitates in NiTi

W. Tirry *, D. Schryvers

Electron Microscopy for Materials Science (EMAT) Physics Department, University of Antwerp (UA), Groenenborgerlaan 171, B-2020 Antwerp, Belgium

Received 9 July 2004; received in revised form 20 October 2004; accepted 31 October 2004
Available online 10 December 2004

Abstract

High-resolution transmission electron microscopy and image-processing techniques are used to measure the strain fields surrounding coherent Ni_4Ti_3 precipitates in an austenitic $Ni_{51}Ti_{49}$ matrix. Images are recorded in the $[1\ 1\ \bar{1}]_{B2}$ and the $[1\ 0\ \bar{1}]_{B2}$ zones, and the $\{1\ 1\ 0\}_{B2}$ interplanar spacings are used to determine the strain induced by both small (50 nm diameter) and large (300 nm diameter) precipitates. From these observations, the maximum strain in the surrounding matrix is mapped and identified as compressive or tensile. Interactions between strain fields of different precipitates are also investigated. A simple model for the observed strain is proposed and compared to the classical Eshelby solution for an ellipsoidal inclusion.

Keywords: Ni_4Ti_3 precipitation; NiTi; HREM; Strain field; Eshelby model

1. Introduction

NiTi alloys with near-equiatomic composition can exhibit shape memory and superelastic properties resulting from an austenite–martensite transformation under temperature change or applied stress. The properties of this transformation are strongly influenced by the presence of Ni_4Ti_3 precipitates in the B2 austenite matrix. The atomic structure and morphology of these precipitates have been investigated before [1–3] and it has been found that, due to the anisotropic change of the unit cell dimensions and lattice parameters, the precipitates form with a lens shape inside the cubic matrix. Their influence on the transformation temperatures and the occurrence of multiple step transformations were mainly investigated by differential scanning calorimetry (DSC) measurements and conventional transmission electron microscopy (TEM) [4–7]. When these precipitates are coherent or semi-coherent, which is the case for a diameter of the central disc up to 300 nm, they can act as nucleation centers for the formation of the R-phase [4,6]. This behavior is explained by the fact that the lattice mismatch between precipitate and matrix induces a stress field in the surrounding matrix. Also the change of Ni concentration in the matrix, due to the higher Ni content in the precipitates, can be expected to have an influence on the local transformation temperatures as is the case for concentration changes at the bulk level [4,8]. Larger precipitates lose their coherency with the matrix and the stress field is partially relaxed by the introduction of interface dislocations [9,10], though they can still act as nucleation centers for the R-phase [4]. In the coherent case, theoretical models are used to calculate which martensite variant is favored next to a particular precipitate, and to predict the morphology and growth of actual precipitate configurations consisting of several precipitates in close proximity and under the influence of an external applied stress [10–12].

* Corresponding author. Tel.: +32 3 265 32 63; fax: +32 3 218 02 57/265 32 57.
E-mail address: wim.tirry@ua.ac.be (W. Tirry).

1359-6454/$30.00
doi:10.1016/j.actamat.2004.10.049

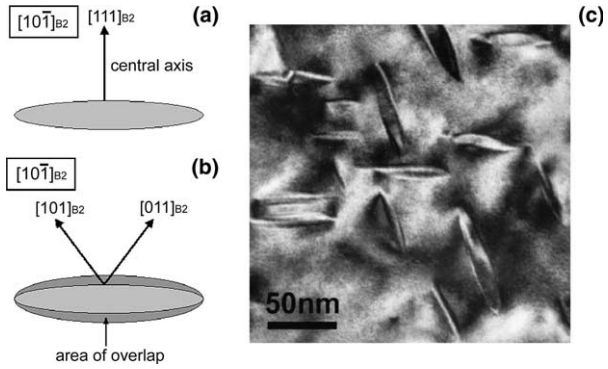

Fig. 1. Schematic drawing of the lens-shaped Ni_4Ti_3 in the two zones: (a) the $[1\,0\,\bar{1}]_{B2}$; (b) the $[1\,1\,\bar{1}]_{B2}$; (c) Typical BF image of Ni_4Ti_3 precipitates with surrounding strain contrast.

These calculations seem to confirm the experimental results, but they are typically based on a theoretical model for the stress field around the precipitate [10,13] as no localized experimental data on the nanoscale is available as yet. In the present work, high-resolution transmission electron microscopy (HRTEM) is used to measure the actual lattice deformations in the matrix around the Ni_4Ti_3 precipitates. To this end, the relative differences in interplanar spacings are determined by fast Fourier techniques applied to the HRTEM images obtained along two simple crystallographic zone directions of the matrix.

The cubic B2 structure of the matrix has a lattice parameter of $a = 0.30121$ nm [11], while for the precipitate the hexagonal description will be used with lattice parameters $a = b = 1.124$ nm and $c = 0.508$ nm [14]. As a result of the decrease in symmetry, eight precipitate variants are possible, the conventional orientation relationship being [1,14]:

$$(1\,1\,1)_{B2}//(0\,0\,1)_{H};\quad [3\,\bar{2}\,\bar{1}]_{B2}//[1\,0\,0]_{H}.$$

In this case the $[1\,1\,1]_{B2}$ direction corresponds to the normal to the central plane of the lens shaped precipitate. In this direction there is a 2.9% contraction in the precipitate relative to the matrix. TEM images indeed reveal this lens shape and conventional two-beam TEM contrast around them indicates the presence of a strain field, as already observed by Bataillard et al. [4]. Fig. 1(a) shows schematic top and side views of a precipitate while the two-beam bright field (BF) TEM image in Fig. 1(b) reveals the stress fields as strong contrast variation in the matrix surrounding the precipitates.

2. Experimental procedures

2.1. Sample preparation

Discs of thickness 300 μm are cut from a 3-mm diameter $Ni_{51}Ti_{49}$ rod and specifically heat treated to form coherent and semi-coherent Ni_4Ti_3 precipitates of different sizes. After homogenization treatment of 1 h at 950 °C in vacuum followed by water quenching, the samples are aged in vacuum for 4 h at 500 °C (sample A) or 450 °C (sample B) and again water quenched. Subsequently, the discs are mechanically ground, followed by double-jet electropolishing in a solution of 93% acetic acid and 7% perchloric acid at 6 °C. This solution yields well-polished samples without preferential etching between precipitates and matrix. The precipitates in samples A measure between 100 and 500 nm in diameter and are located mainly in the vicinity of grain boundaries and oxide or carbide particles. The precipitates in samples B are more finely distributed and their diameter is smaller than 100 nm.

2.2. Method for measuring interplanar spacings

High-resolution images are obtained with a top-entry JEOL 4000EX electron microscope equipped with a LaB_6 filament and operating at 400 kV. HRTEM micrographs are recorded on standard photographic plates in order to capture as much information as possible in a single image. Lattice deformations or strain are determined by measuring and comparing interplanar spacings at different positions in the HR image. The interplanar spacing of a crystallographic plane is measured by applying a fast Fourier transformation (FFT) to the digitized HR image. Then, the pixel distance is measured between the central spot (spatial frequency = 0) and that of the crystallographic plane under consideration.

As the expected deformations are relatively small, special care is required in order to obtain accurate and interpretable data. In practice, the micrographs are digitized with an appropriate scanner either directly from the negative or from an optical enlargement. The resulting image file is left uncompressed with original gray values. Possible artifacts introduced by the enlargement and/or scanner are compensated for by calibrating both procedures with images from undistorted matrices. In fact, distortions should only be measured at a perpendicular angle to the direction of motion of the scanner CCD array. Indeed, the discontinuous movement of the CCD array introduces false deformations in the direction of motion, which is why no two-dimensional displacement maps are made. Then, a window of (512, 512) pixels is moved over a constant distance (e.g. 128 pixels) as indicated in Fig. 2(a) and at each location the FFT is calculated. In order to avoid streaking in the FFT due to the sharp edges of the selection window, a mask filter is applied and the FFT is calculated as shown in Fig. 2(b). The matrix thus obtained is symbolized by FI.

To be able to accurately measure the distances between spots for each FFT window, their centers need

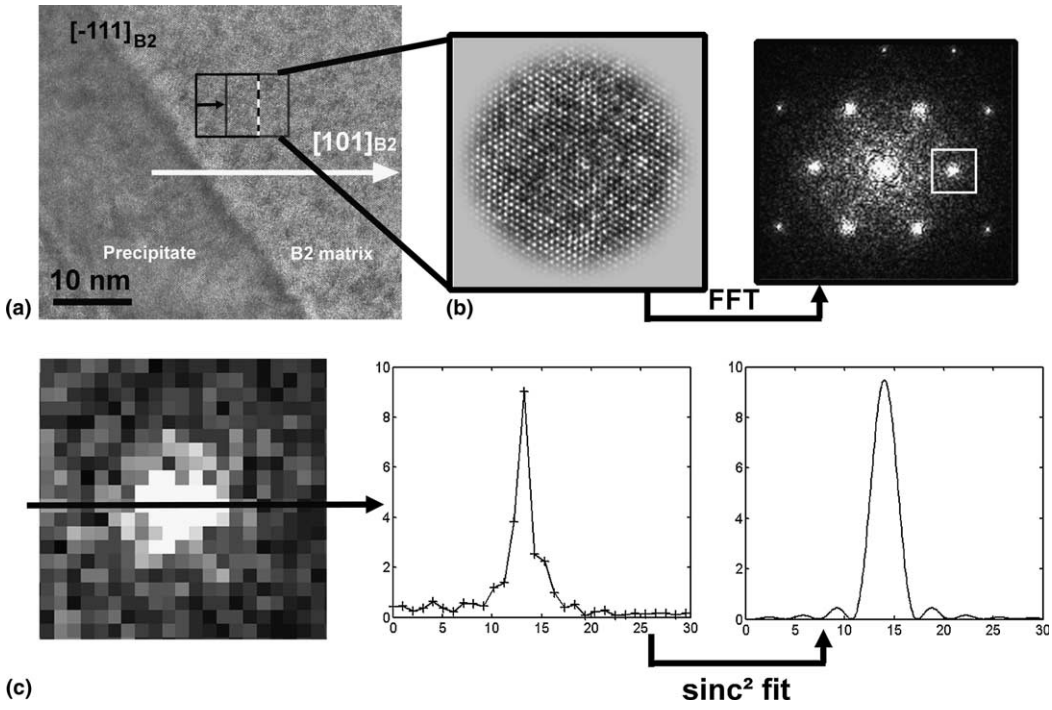

Fig. 2. (a) High-resolution micrograph of precipitate and matrix including the selected windows. (b) FFT of a 512×512 pixel selection window after superimposing a circular mask filter. (c) Maximum position of spot determined by fitting a $\sin c^2$ function with visualisation of a one-dimensional slice through the spot.

to be determined. In principle, the center of a spot should coincide with the highest intensity, but in practice this is not always the case. This is due to the fact that noise or other artifacts can alter the intensity of each pixel. To locate the real maximum, a mathematical model is proposed and fitted to the $\sqrt{\mathrm{FI} \times \mathrm{FI}^*}$ data. In the case of a two-dimensional atomic resolution image, the sinc^2 (sqrt($x^2 + y^2$)) is a good model for describing the intensity of the spots [15], certainly for the central part of interest. This is shown in Fig. 2(c), which compares a profile through the spot with the corresponding fitted sinc^2 function. However, a two-dimensional fitting procedure still requires long computation times to converge towards a satisfactory solution. Fortunately, a comparable degree of accuracy can be obtained by combining two one-dimensional sinc^2 fittings in sequence. The maximum value pixel serves as a starting point through which one-dimensional sinc^2 functions in the x and y directions are fitted. The position of the maximum of the fit along the $x(y)$-direction is retained as the $x(y)$ coordinate for the position of the spot maximum. In this manner, an optimized position for the x and y coordinates of the maximum is obtained with subpixel accuracy. A similar one-dimensional fitting procedure is applied in the DALI program [16] to refine the position of atom columns in a real space image.

The measured interplanar spacing of a particular plane in the precipitate is chosen as a reference. Differences Δd in interplanar spacing are then given as a percentage relating to this reference distance, e.g. a Δd of 3% means that the measured interplanar spacing is 3% larger than the corresponding spacing in the precipitate. The differences can then be represented in a (Δd – distance) graph, as shown in Fig. 3. To determine the actual strain of the matrix regions, these figures can further be renormalized with respect to the corresponding spacing of the unstrained matrix.

When measuring interplanar spacings from HRTEM images, one needs to be wary of several imaging artifacts that can shift lattice fringes without any distortion or composition change in the sample [17–19]. However,

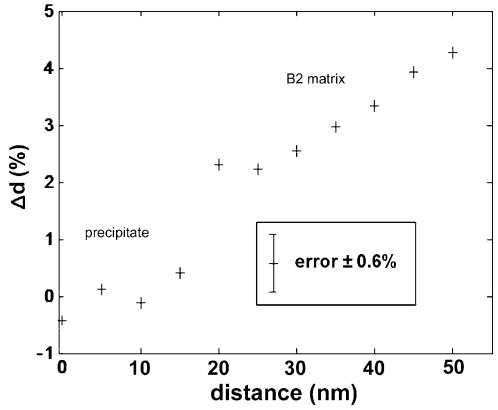

Fig. 3. Measured $(1\,0\,1)_{B2}$ $\Delta d(\%)$ in the $[1\,0\,1]_{B2}$ direction given by the white arrow in Fig 2(a).

as we are dealing with symmetric crystallographic zone orientations of a centro-symmetric unit cell, most of these effects are cancelled out [20]. What remains is a possible shift in the position of the lattice image with respect to the projected sublattices in the unit cell with changing sample thickness and minor effects due to inevitable misalignments. The first effect occurs when the thickness changes by more than a given amount in a well-defined thickness regime. In such an event, the contrast of the image might be inverted, i.e. the bright dots may shift from the real lattice positions to in-between positions or from one set of atom columns to another, leaving the periodicity in the image unaffected. In practice, such an image shift is never observed within the regions of interest, which confirms that the samples are smoothly polished. Moreover, such an effect would only cause the respective FFT reflection to exhibit two maximums, separated by a distance reversibly depending on the window size. Simulations show that the fitted sinc^2 still reveals the proper center of the main reflection within the limits of precision (see also following section). The second effect is minimized by taking extra care in performing the alignment procedures, with any remaining deviations being covered by the estimate of the standard deviation as explained below.

The precision of the present procedure is estimated by means of an image of a region where no strain or distortions are expected, but which is otherwise comparable in HRTEM image code with the analyzed images including precipitates. The interplanar spacing is determined in different locations of the central part of the negative, yielding a standard deviation of 0.6% on the mean value for this distance. This means that, for an HRTEM image of an undistorted region taken under the same conditions as the analyzed images (i.e. defocus, magnification, alignment, thickness range, composition homogeneity, etc.) all effects leading to changes in lattice fringes, resulting either from imaging artifacts or from inhomogeneities in the matrix, do not produce changes in the lattice parameter of more than 0.6% within the conventional definition of a standard deviation. This value is then further used as precision on all subsequent measurements. Moreover, this procedure allows us to identify the validity boundaries of the central part of the negative. The spatial resolution of the present procedure is 5 nm, which corresponds to the window size and magnifications used. In order to allow processing of large negatives and multiple regions this procedure is automated and implemented in MATLAB® functions.

3. Results

Given the lattice parameters and crystallographic relations between the matrix and precipitates, the $[1\,0\,\bar{1}]_{B2}$ and $[1\,1\,\bar{1}]_{B2}$ zones are considered to be of greatest interest, as they will reveal the largest deformations. Moreover, in the $[1\,0\,\bar{1}]_{B2}$ zone, the $(1\,1\,1)_{B2}$ central plane is observed edge-on, so we may assume that a major part of the interface between the matrix and precipitate is also viewed edge-on. In the $[1\,1\,\bar{1}]_{B2}$ zone, however, this plane is at a 19.47° angle with the incident beam, resulting in an overlap between matrix and precipitate that depends on the total thickness of the sample and the size and location of the precipitate. Still, the results of the latter case are described first, as the HRTEM images are typically of a better quality due to overall larger lattice spacings.

3.1. $[1\,1\,\bar{1}]_{B2}$ observations:

In samples A, precipitates with a diameter of 200–300 nm are selected for coherency reasons, as explained above. In a $[1\,1\,\bar{1}]_{B2}$ orientation, two of the three edge-on $\{0\,1\,1\}_{B2}$ families of planes ($(1\,0\,1)_{B2}$ and $(0\,1\,1)_{B2}$) have a theoretical difference of 2.01% between the corresponding interplanar spacings of the precipitate and the unstrained matrix. The measured percentage difference for one of these interplanar spacings, $(1\,0\,1)_{B2}$ as indicated in Fig. 2(a) and measured along $[1\,0\,1]_{B2}$ in an area around the central part of the precipitate, is given in Fig. 3. At a distance of 50 nm from the center of the precipitate, Δd peaks at about 4%, implying an expansive strain of approximately 2% with respect to the unstrained matrix. However, it is unclear from this image whether this value represents a true maximum or whether the expansive strain reaches even higher values at a further distance from the precipitate. Close to the interface, the measured Δd is about 2%, i.e. the unstrained matrix, and increasing linearly up to a maximum of 4%. On the other hand, at the tip of the precipitate, the $(1\,0\,1)_{B2}$ interplanar spacing is found to be smaller than the corresponding value for the matrix, implying compression. This is noticeable in the contour plot in Fig. 4, where all measurements of the $(1\,0\,1)_{B2}$ interplanar spacing are combined.

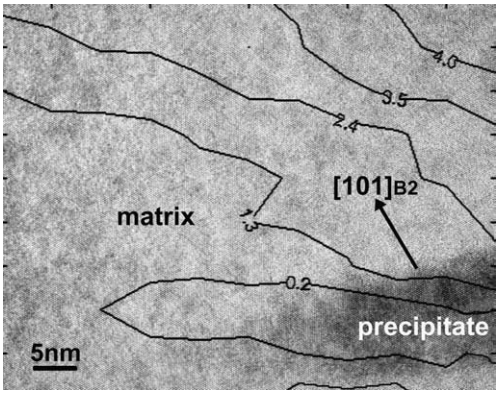

Fig. 4. HRTEM image of the tip of a Ni_4Ti_3 precipitate in $[1\,1\,\bar{1}]_{B2}$ zone orientation. The contours give the Δd(%) for the $(1\,0\,1)_{B2}$ planes.

The interplanar spacing of the third $\{0\,1\,1\}_{B2}$ family of planes $(1\,\bar{1}\,0)_{B2}$, which lies perpendicular to the central axis of the precipitate in the present crystallographic zone, has a theoretical mismatch of only 0.38%,which is confirmed by the fact that no difference between these interplanar spacings is measured.

For samples B, we examined precipitates with a diameter around 50 nm. In this case, there are more precipitates and two of the same variant can even be examined in a single micrograph. In the example in Fig. 5, two parallel precipitates are found about 40 nm apart. The largest Δd for $(1\,0\,1)_{B2}$ of 3.3%, and thus a maximum matrix strain of 1.3%, is found at a distance between 5 and 10 nm of the interface of the left precipitate. When moving further away, Δd decreases sharply. After 10 nm, we reach the unstrained matrix with the expected Δd of 2% with respect to the precipitate. Close to the right precipitate, the strain increases again leaving a flat unstrained matrix of about 20 nm in width in between the two precipitates. The two-dimensional shape of the strain field is visualized in Fig. 6 by plotted contour lines. The maximum strain is located close to the central part of the interfaces, while at the tips we encounter a smaller strain, a compression even, i.e. a Δd value smaller than 2%.

As mentioned above, there is an area of matrix-precipitate overlap when looking in the $[1\,1\,\bar{1}]_{B2}$ zone, so that observations close to what appears to be the interface might be difficult to interpret. Image simulations (using Mactempas) indicate that the lattice images observed in the present zone may be expected for samples of thickness 10–15 nm, corresponding with an overlap around 5.3 nm, which is certainly closer to the precipitate than the maximum strain location at 50 nm in samples A. This implies that images suffering from overlap would only occur in the first part of the increment towards the maximum in samples B. Moreover, although the image from these areas may be distorted due to interference between the two structures, simulations show that the observed interplanar spacing for lattice

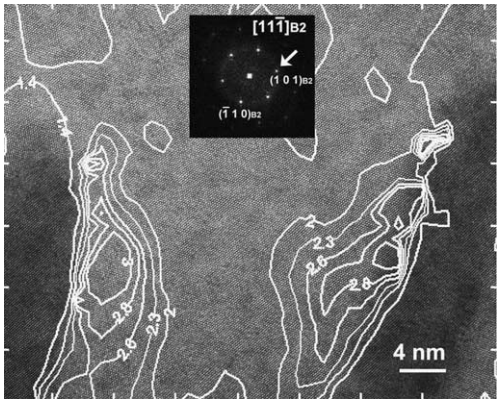

Fig. 6. Contour plot of Δd(%) for the $(1\,0\,1)_{B2}$ planes in between two small precipitates observed in $[1\,1\,\bar{1}]_{B2}$ zone orientation.

images clearly reveal the matrix can never be larger than the real spacing, as expected. The maximum for the observed Δd, even in the case of the small precipitates, is therefore real and not an artifact. It is reached at a distance d from the precipitate, depending on the size of the latter.

3.2. $[1\,0\,\bar{1}]_{B2}$ observations

Similar results are obtained when viewing the matrix in the $[1\,0\,\bar{1}]_{B2}$ zone. For the $(1\,0\,1)_{B2}$ planes, the measured strain again increases with distance from the precipitate. In the example in Fig. 7, obtained from a sample A, Δd is plotted in between as well as on one side of adjacent tips of two precipitates of the same variant type. Between these tips, the strain for the $(1\,0\,1)_{B2}$ planes is about 1% larger than at the same distance at the other side of the precipitate. At this side of the tip and close to the interface, Δd remains smaller than the lattice mismatch of 2%, again implying local compression of the matrix. At about 30 nm from the center of the rightmost precipitate, a lattice mismatch of 2%, i.e. unstrained matrix, is reached but unfortunately no

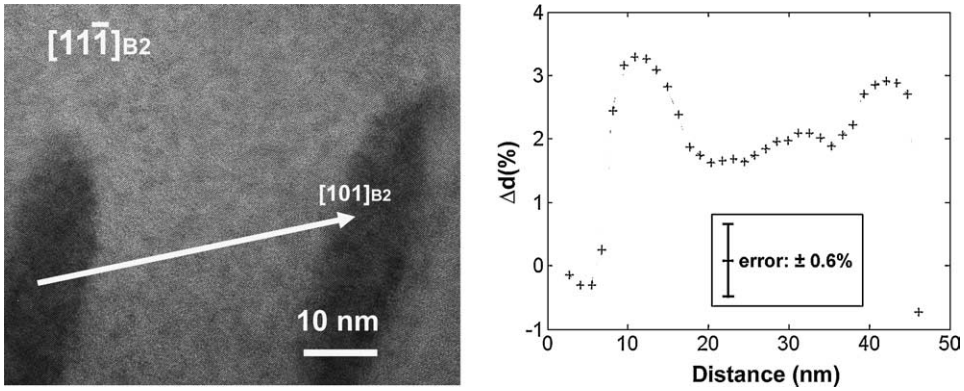

Fig. 5. $(1\,0\,1)_{B2}$ profile between two small precipitates 40 nm apart.

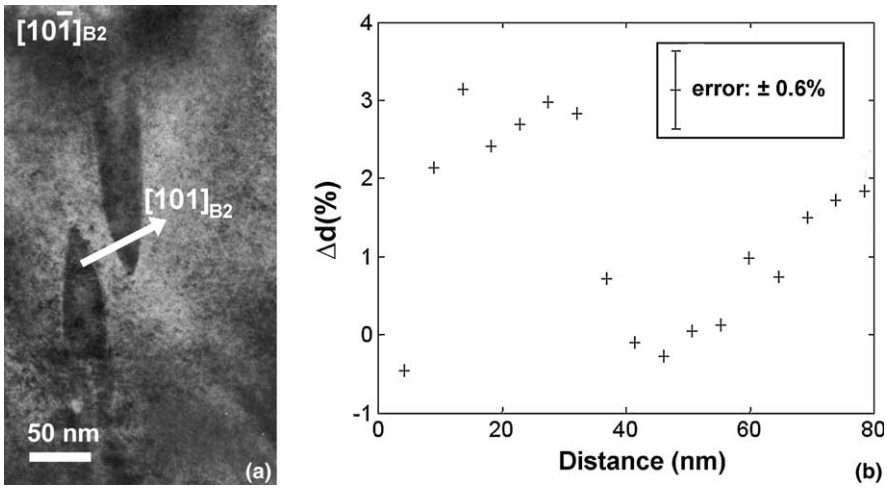

Fig. 7. (a) Two precipitates of the same variant type with tips very close to each other and observed in [1 0 $\bar{1}$]$_{B2}$ zone orientation. The straining of the (1 0 1)$_{B2}$ planes is measured according to the white arrow and given in (b).

measurements could be made to find the exact location of the maximum strain, due to a limited precision closer to the edges of the negative.

As regards the small precipitates in samples B, again several precipitates can be observed at once. As in the [1 1 $\bar{1}$]$_{B2}$ zone, the largest strains for the (1 0 1)$_{B2}$ planes are found close to the interface and between precipitates of the same variant type, while at the tip of a precipitate we observe compression.

4. Discussion

The present work focuses on the lattice strains induced in a Ni-rich Ni–Ti matrix when Ni_4Ti_3 precipitates are formed by an appropriate annealing treatment. Using [1 0 $\bar{1}$]$_{B2}$ and [1 1 $\bar{1}$]$_{B2}$ zone HRTEM images of precipitates embedded in a surrounding matrix, relative differences in lattice spacings are measured. Comparison of these values with unstrained regions or with the theoretical lattice parameters yields the matrix deformations. In principle, the continuous deformation effect on the matrix by a precipitate with other lattice parameters than the matrix will increase when the precipitate grows coherently, until coherency is lost and interface dislocations occur. Thus, the first obvious choice is to look for coherent precipitates with the largest possible dimensions, which in this case is a central plane diameter of approximately 300 nm. Such precipitates were found in samples A, treated for 4 h at 500 °C. As Figs. 3 and 4 show, large strained regions are indeed found alongside such precipitates. However, as the minimal microscope magnification for the required resolution is 500 K and distortion-like artifacts are often found at the edges of a micrograph, only a small part of the surrounding matrix can be observed in a single micrograph. Indeed, the matrix part that could be measured in the example in Fig. 2 extends to only about 50 nm aside the precipitate–matrix interface. In this case, we observe a linearly increased straining of the (1 0 1)$_{B2}$ and (0 1 1)$_{B2}$ planes away from the interface. This straining should peak, after which the lattice should relax until eventually reaching the unstrained matrix. As no maximum is observed in the present example, we were unable to determine how far the straining reaches. It is clear, however, that the maximum strain is not located at the interface itself but at a distance from it, even when taking into account the overlap region between precipitate and matrix with an expected larger inaccuracy in the measurements. As the strain field should only compensate for the introduced lattice mismatch, the overall (or mean) deformation, i.e. including the precipitate, should be zero. Thus, for a given precipitate size, the larger the maximum strain, the shorter the strain field and the closer the distance between unstrained matrix and precipitate.

For smaller precipitates, as in Fig. 5, in which the lattice deformations indeed relax back to the unstrained matrix even though both precipitates are only 40 nm apart, this can be confirmed by taking the mean value of the entire strain curve and assuming the same curve on the opposite side on the basis of symmetry considerations. The mean value obtained for Δd is 1.9%, which indeed equals, within the experimental margin of error, the lattice mismatch of 2% for these planes. We may thus conclude that the mean interplanar distance for the (1 0 1)$_{B2}$ and (0 1 1)$_{B2}$ planes is equal to that of the unstrained B2 matrix and that the overall deformation is zero. In other words, the strain field fully compensates for the lattice mismatch between precipitate and matrix and is located very close to the interface.

Besides the maximum value and the location of the most strained part, the basic shape of the strain field can also be proposed, as in Fig. 8. This shape results

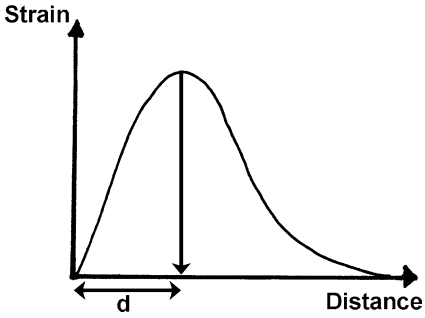

Fig. 8. Proposed strain field for the matrix starting at the precipitate–matrix interface. The maximum is reached at a distance d from the interface.

from a combination of observations of large and small precipitates. Due to the limited resolution of the window technique applied, the precision of measurements in the first 5 nm from the interface is affected by the inclusion of both precipitate and matrix in the FFT window. Thus, for the part closest to the interface, the measurements of the large precipitates are more relevant for a general model. Further away from the precipitate, the maximum deformations are observed only in the case of the smaller precipitates, so this part of the model relates to these situations.

The curve in Fig. 8 results from measurements in a direction perpendicular to or at a wide angle with the interface plane and close to the central area of the precipitate. At the tip of a precipitate, the measured values for these Δd are smaller than the lattice mismatch, indicating matrix compression, usually below 1%, in these areas.

The simple graphical schematic in Fig. 9, based on a drawing by Tadaki [1], reveals the expected strain effects on the $\{0\,1\,1\}_{B2}$ type planes as selected in the present research. The schematic shows that, at the tips, compression of the $\{0\,1\,1\}_{B2}$ planes may indeed be expected in order to adapt to the smaller interplanar spacing of the precipitate, whereas, perpendicular to the central part of the interface, we observe expansion. Moreover, the compression region is strongly located

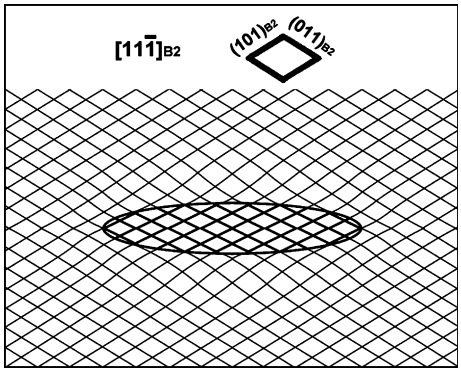

Fig. 9. Drawing of the proposed lattice deformation of $\{1\,1\,0\}_{B2}$ planes surrounding the precipitate (after Tadaki et al. [1]).

in front of the tip, while expansion begins immediately alongside the precipitate and continues away from the tip, with the curvature of the interface decreasing sharply. This explains the increased strain between the two precipitates in Fig. 7, even though their tips are in close proximity.

The present nanoscale experimental detail can be compared with the conventional TEM results for larger precipitates obtained by Bataillard et al. [4]. As can be seen in Fig. 9 in [4], the stress induced R-phase region surrounding the precipitate extends to about 300 nm from the precipitate, which explains why no maximum was observed for our largest precipitates.

The most commonly used and widely accepted analytical solution for the problem of an ellipsoidal inclusion in an elastic matrix is based on the Eshelby approach. A complete solution for the strain and stress fields around such an inclusion is given in [21]. Eshelby's solution shows that the interior stress and strain field is uniform within the inclusion. Indeed, the measurements inside the precipitate exhibit no differences in interplanar spacing, which justifies its use as a reference distance. The solution for the strain field in case of exterior points is more complex and is given by the basic equation

$$\varepsilon_{ij}(\mathbf{x}) = D_{ijkl}(\mathbf{x})\varepsilon^*_{kl},$$

where ε^* is the eigenstrain for the elliptical inclusion and the D tensor is dependent on the position $\mathbf{x}$ in the surrounding matrix. The extensive computation of this D tensor is done with a program based on that developed by Gall [10]. The solution is valid for isotropic ellipsoidal inclusions in an isotropic infinite body, with the same elastic moduli for the matrix and the inclusion.

If the three basic axes of the ellipsoid are defined by $a1$, $a2$ and $a3$, then for Ni_4Ti_3 $a1 = a2 > a3$. A calculation is made for a precipitate with parameters $a1 = a2 = 50$ nm and $a3 = 10$ nm, which is the approximate size of the two precipitates in Fig. 5, and using an eigenstrain ε^* as defined in [11]. This eigenstrain is valid in the principle coordinate frame defined by: $[1\,\bar{1}\,0]_{B2}$, $[1\,1\,\bar{2}]_{B2}$ and $[1\,1\,1]_{B2}$.

$$\varepsilon^*_{i,j} = \begin{pmatrix} 0.014 & 0 & 0 \\ 0 & 0.014 & 0 \\ 0 & 0 & -0.029 \end{pmatrix}.$$

The computed strain for the $(1\,0\,1)_{B2}$ planes in the $[1\,0\,1]_{B2}$ direction is given in Fig. 10. The computed curve has the same shape as the one deduced from the measurements in Fig. 8, although comparison of the magnitudes of the theoretical strain fields with the measured values reveals substantial differences. Indeed, the measured strain values are up to 10 times larger and the experimentally observed maximum is located closer

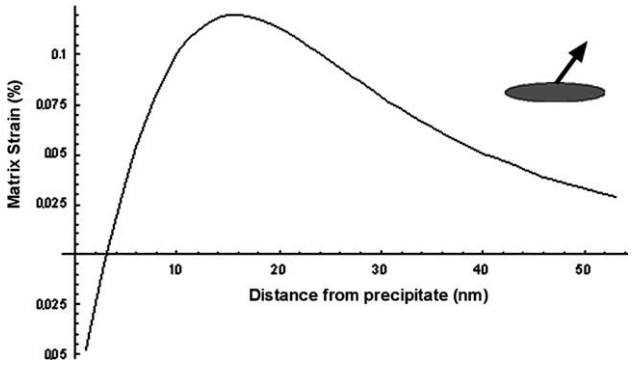

Fig. 10. Calculated strain curve for the $(1\,0\,1)_{B2}$ planes in the $[1\,0\,1]_{B2}$ direction.

to the interface. This may be due to the assumption of an equal stiffness for precipitate and matrix. Since the elasticity modulus of Ni_4Ti_3 has not yet been measured, this discrepancy between theoretical and experimental values might indicate that this modulus of the precipitate is not equal to that of the matrix. Interactions between elasticity moduli and shape and orientation of precipitates in a matrix are indeed known [22,23]. Furthermore, the actual shape of the precipitates deviates from the ideal ellipsoid, though one would only expect to find notable differences around the tips. In such a case, the computation of the strain fields is more complex and the solution is not considered in the present paper. Although the magnitudes are not the same, the positions of tensile and compressive strain are as expected: compression at the tips and maximum tensile strain along the central axis, as is apparent from the contour plot in Fig. 11, showing the straining of the $\{1\,1\,0\}_{B2}$ planes when observed in the $[1\,1\,\bar{1}]_{B2}$ zone orientation. If we make this calculation for a larger precipitate, we find that the distance d of the maximum increases, leading to a similar conclusion as that based on the measurements.

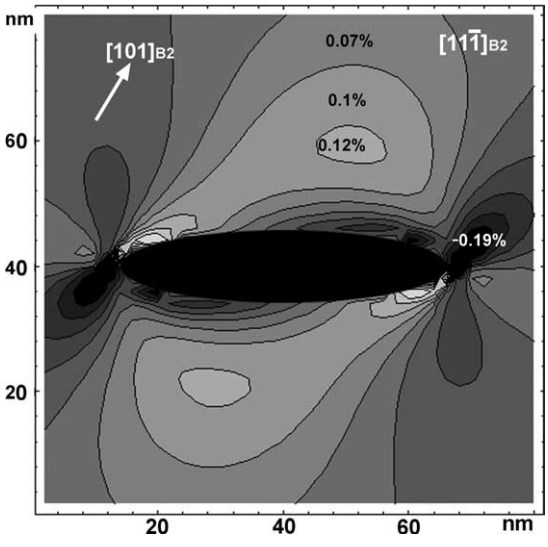

Fig. 11. Calculated strain plot for the $(1\,0\,1)_{B2}$ planes in the $[1\,0\,1]_{B2}$ direction.

The present experimental results confirm the concept of local lattice strains surrounding the Ni_4Ti_3 precipitates and considered to be at the origin of the nucleation of the R-phase variants alongside these precipitates. However, comparison of the measured strain values with those obtained with an Eshelby approach clearly shows that if we take into account the influence of the precipitates on the martensitic transformation at the micro- and nanoscopic scale, a model based on the conventional Eshelby approach with an ellipsoidal inclusion does not suffice. Moreover, any additional influence from local concentration variations due to the growth of the Ni-rich precipitates can still not be ruled out.

5. Conclusions

The straining in a body-centred cubic Ni–Ti matrix surrounding Ni_4Ti_3 precipitates is studied by means of HRTEM. Using image-processing techniques based on fast Fourier transformations, strain fields in the surrounding matrix are determined for the $\{1\,1\,0\}_{B2}$ planes along the $\langle 1\,1\,0\rangle_{B2}$ directions. The maximum expansive strain is not located at the interface of the precipitate, but at a distance *d*, increasing with the size of the precipitate, which lends support to the concept of R-phase nucleation near precipitates due to local lattice strains. In front of the tips of the precipitate, the matrix undergoes compressive strain, as expected. In between two small precipitates only 40 nm apart, an unstrained matrix of 20 nm wide is observed. Comparison of our measurements with the Eshelby solution suggests that the assumption of equal elasticity modulus for precipitate and matrix may be false.

Acknowledgements

This work is supported by the Trade and Mobility Research Programme of the EEC under the project FMRX-CT98-0229 (DG12-BDN) entitled ''Phase Transitions in Crystalline Solids''. We thank K. Gall for supplying the source code of his Eshelby program, which was subsequently adapted to this special case, and for his useful suggestions. The measurements to determine the exact composition and lattice parameter of the NiTi samples were made by J. Khalil-Allafi, W. Shmall and T. Reinecke. We thank A. Rosenauer for his suggestions regarding possible high-resolution imaging artifacts.

References

[1] Tadaki T, Nakata Y, Shimizu K, Otsuka K. Trans JIM 1986;27:731.
[2] Nishida M, Wayman CM. Mater Sci Eng 1987;93:191.
[3] Nishida M, Wayman CM, Honma T. Metal Trans A 1986;17:1505.
[4] Bataillard L, Bidaux J-E, Gotthardt R. Phil Mag A 1998;78:327.
[5] Khalil-Allafi J, Dlouhy A, Eggeler G. Acta Mater 2002;50:4255.
[6] Filip Peter, Mazanec Karel. Scripta Mater 2001;45:701.
[7] Zel'dovich V, Sobyanina G, Novoselova TV. J Phys IV France 1997;7:299.
[8] Khalil Allafi J, Ren X, Eggeler G. Acta Mater 2002;50:793.
[9] Zou WH, Han XD, Wang R, Zhang Z, Zhang W-Z, Lai JKL. Mater Sci Eng A 1996;219:142.
[10] Gall K, Sehitoglu H, Chumlyakov YI, Kireeva IV, Maier HJ. J Eng Mat Technol 1999;121:19.
[11] Li DY, Chen LQ. Acta Mater 1997;45:471.
[12] Li DY, Chen LQ. Acta Mater 1997;46:639.
[13] Michutta J, Carroll MC, Yawny A, Somsen Ch, Neuking K, Eggeler G. Mater Sci Eng A 2004;378:152.
[14] Somsen C. Mikrostrukturelle Untersuchungen an Ni-reichen Ni–Ti Formgedächtnislegierungen. Shaker Verlag; 2002.
[15] Gonzalez RC, Wintz P. Digital image processing. 2nd ed. Reading (MA): Addison-Wesley; 1987.
[16] Rosenauer A, Gerthsen D. Atomic scale strain and composition evaluation from high-resolution transmission electron microscopy images. Advances in imaging and electron physics. vol. 107. p. 131.
[17] Smith David J, Saxton WO, O'Keefe MA, Wood GJ, Stobbs WM. Ultramicroscopy 1983;11:263.
[18] Hÿtch MJ, Plamann T. Ultramicroscopy 2001;87:199.
[19] Spence JCH. Experimental high-resolution electron microscopy. Oxford: Clarendon Press; 1981.
[20] Hÿtch MJ. Scanning Microsc 1997;11:53.
[21] Mura T. Micromechanics of defects in solids. Boston: Nijhoff; 1982.
[22] Choy Jun-Ho, Lee Jong K. Mater Sci Eng A 2000;285:195.
[23] Mueller R, Gross D. Comp Mater Sci 1998;11:35.